Final Report for Award DE-FG02-00ER54583

Report period: Aug 15, 2000-Aug. 14, 2007

Principal Investigator:
Uwe Kortshagen, Ph.D., Professor of Mechanical Engineering and Physics,
University of Minnesota, 111 Church Street S.E., Minneapolis, MN55455.

Co-Principal Investigator:
Joachim Heberlein, Ph.D., of Mechanical Engineering,
University of Minnesota, 111 Church Street S.E., Minneapolis, MN55455.
Steven L. Girshick, Ph.D., Professor of Mechanical Engineering,
University of Minnesota, 111 Church Street S.E., Minneapolis, MN55455.

Post-doctoral Associates:
Dr. Konstantin Orlov

Graduate Research Assistants:
Curtis Anderson
Lorenzo Mangolini
Lavanja Ravi
Siri Thompson
Giovanni Visentin
Sarah Warthesen
Peng Zhang

Research Activities:

This project was funded over two periods of three years each, with an additional year of no-cost extension. Research in the first funding period focused on the physics of uniform atmospheric pressure glow discharges, the second funding period was devoted to the study of the dynamics of nanometer-sized particles in plasmas.

I. Atmospheric pressure glow discharges

The first goal of our research was to understand the physical mechanisms responsible for a formation of the homogeneous barrier discharge mode. Atmospheric pressure glow discharges in helium have been reported to produce radially uniform plasmas and to show one single current pulse per half cycle of the AC high voltage. However, in other studies the appearance of multiple periodic peaks per half cycle has been reported as well that was interpreted as oscillation of the cathode sheath based on a simplified numerical model. Our studies presented below indicate that this interpretation is incorrect.

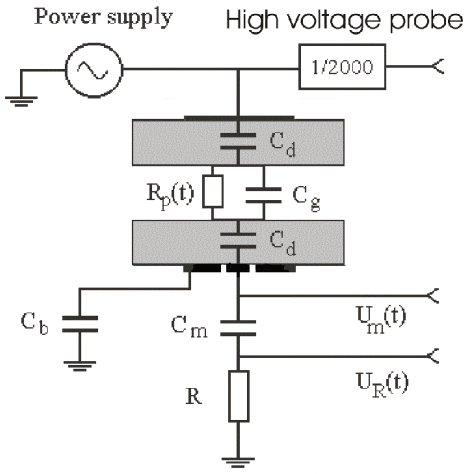

FIGURE 1. Electrical measuring circuit schematic and plasma equivalent circuit.

Our experimental studies in this project focused on the study of the breakdown mechanism, the appearance of multiple current peaks, and on the influence of the dielectric on the spatial discharge uniformity. The experimental apparatus constructed under this grant consists of a stainless steel chamber that is evacuated to a pressure of few mTorr before being filled with helium at a pressure of 760 Torr. Two aluminum electrodes with 4 cm in diameter are mounted on insulating holders to prevent arcing with the chamber walls. Different dielectric plates can be placed on them. A schematic of the electrodes and the electrical measuring circuit is shown in figure 1. The inter-electrode distance can be adjusted using a micrometric linear operator. A high voltage amplifier supplies the power; this device allows us to vary the applied voltage over a wide range of frequencies and to apply different waveforms. The lower electrode is segmented with a central part of $1cm^2$ used to measure the current and the external part serving as guard ring that minimizes edge effects. The current signal from the discharge is measured through a shunt resistor. A capacitor C_m in series with the circuit is used to measure directly the voltage drop across the dielectric barriers. For side-on optical imaging measurements we have used an intensified CCD camera that allows a minimum exposure time of 10 nsec.

In our studies, we focused on the radial evolution of the discharge during breakdown. Initially, we used 3.3 mm thick glass plates with $\varepsilon_r = 4.6$ and we observed that the second current pulse per half cycle is connected to the radial non-uniformity of the charge deposited on the dielectrics. Figure 2 shows the typical current signal from the discharge and the relative light emission under these conditions. During the first pulse we observed the light emission spreading from the center towards the edges of the electrode; during the second pulse we observed an ionization wave proceeding inward. Multiple diffuse filaments appeared during this stage of breakdown. We interpret this effect as follows: the first ionizing wave deposits enough charge to lower the gap voltage

such that the discharge distinguishes. The charge is deposited non-uniformly with a maximum at the discharge center. If the applied voltage continues to rise and the breakdown voltage is reached again a second pulse is observed, this time starting from outside where less charge was deposited and consequently the gap voltage is slightly higher than in the center. Our measurements showed no evidence of an oscillation of the cathode layer as suggested in ref. [2].

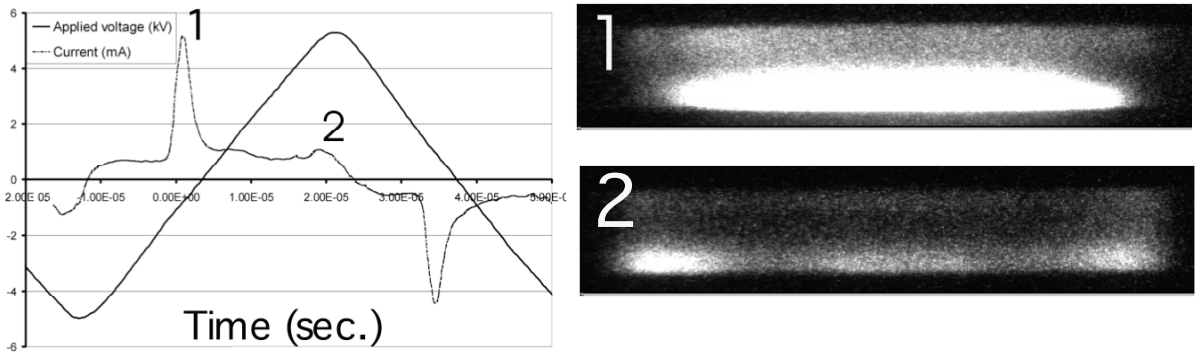

FIGURE 2. Two-puls current signal and light emission in the middle of each pulse, 3.3 mm glass dielectrics.

The discharge structure observed in our studies appeared strikingly different from the one reported in ref. [1]. In particular, our experiments did not show the typical glow discharge structure of a cathode layer, Faraday dark space, and positive column that was observed in ref. [1]. The main difference in both studies is the dielectric used. While in our study a glass dielectric was used ($\varepsilon_r = 4.6$, thickness 3.3 mm) in ref. [1] alumina plates with ($\varepsilon_r = 9$, and a thickness of 0.6 mm were used. Hence the impedance of our glass dielectrics is by a factor of 10 larger than that of the dielectrics in ref. [1]. In order to test the assumption of the decisive influence of the dielectric, we performed additional experiments with 0.635 mm thick alumina plates.

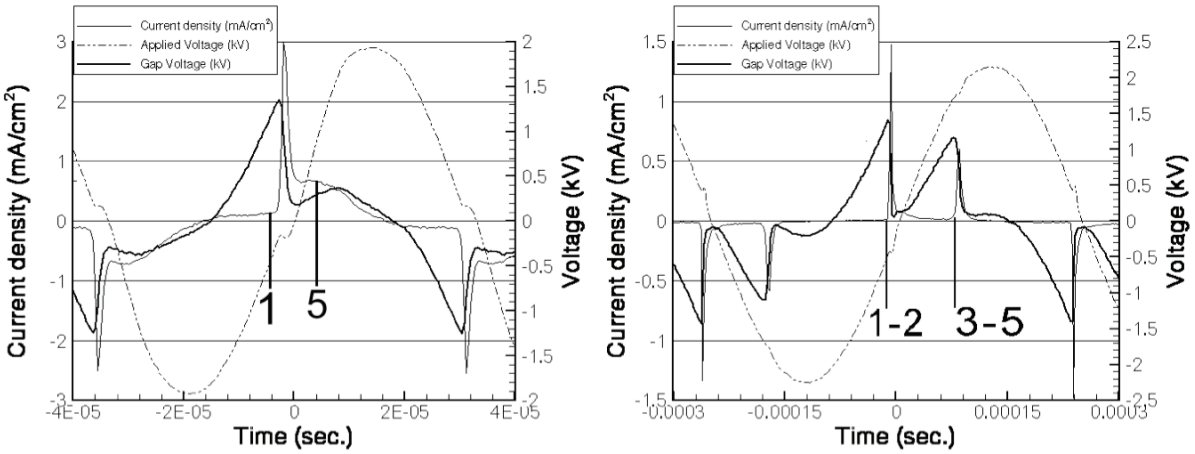

FIGURE 4. Electrical characterization of atmospheric pressure glow discharge with 0.635 mm thick alumina plates; applied frequency is 15 kHz in the left diagram, 2 kHz in the right one; gap is 5 mm in both cases.

In figures 4 and 5 we show experimental results obtained by using the alumina dielectrics for the same gap width as with the glass dielectrics. As in the case with glass dielectrics, we were able to operate the discharge in modes with one current pulse per half period at high frequencies and two current pulses at lower frequencies. The discharge light emission shows considerable differences from the case with glass dielectrics. The left hand side of fig. 5 shows the light emission during the one current pulse case. The distinct structure of a cathode layer, Faraday dark space, and positive column is now well visible. As in previous studies with glass plates we observe that the discharge spreads in radial direction while preserving the axial structure. The right hand side of figure 5 shows the light emission during the lower frequency case. The upper two pictures are taken during the first current pulse, the lower three during the second current pulse. Again, we find a behavior similar to the one observed in ref. [3] and discussed above for fig. 2. During the first current pulse the discharge spreads in radial direction. Again the charge deposited on the dielectric seems to be non-uniform and maximum in the discharge center, since the second current pulse ignites in the discharge periphery. An inward moving ionization front can clearly be observed.

In conclusion, we showed that qualitatively similar behavior is found for glass and alumina dielectrics with respect to the multi-current behavior of the discharge and the radial evolution of the discharge breakdown. Clear differences are seen in the axial structure of the discharge. While a pronounced structure of cathode layer, Faraday dark space, and positive column can be seen with alumina dielectrics, this structure is absent for glass plates. The reasons for this difference are currently under investigation.

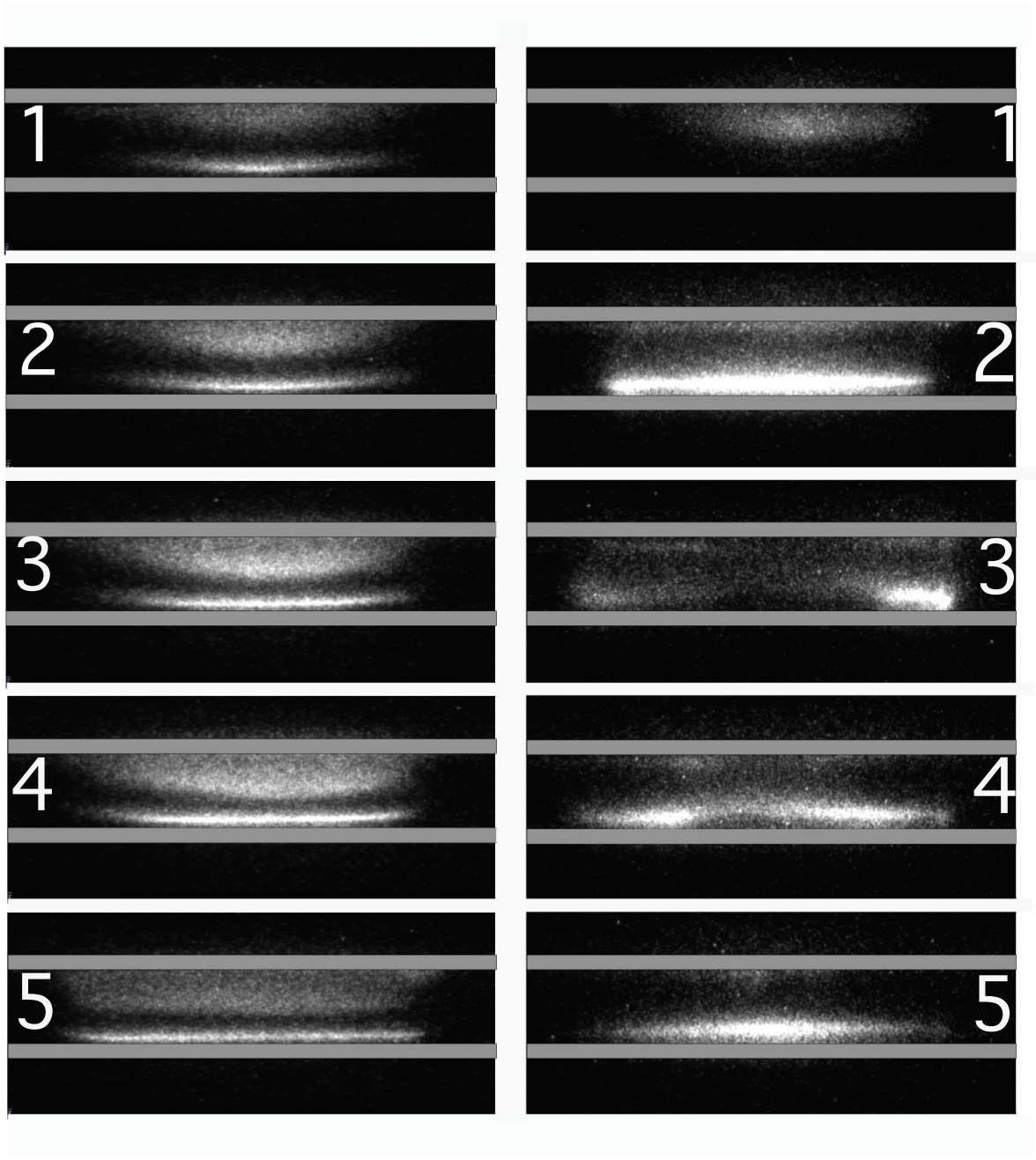

FIGURE 5. Light emission from atmospheric pressure glow discharge during positive half cycle; on the left is single current pulse case (15 kHz), on the right the two pulses case (2 kHz). Dielectric barriers are 0.635 mm thick alumina plates. See figure 4 for the respective current signals. Exposure time is 15 nsec for the sequence on the left, 100 nsec for the sequence on the right.

In later studies, we have achieved new insight into the discharge mechanism through time-resolved two-dimensional spectroscopy. The time-dependence of the spectral emission of an atmospheric pressure glow discharge in helium with impurities were studied. Emissions from He I ($3s^3S \rightarrow 2p^3P$: λ = 706.5 nm) and N_2 ($C^3\Pi_u \rightarrow B^3\Pi_g$: λ = 337.1 nm) was used to qualitatively map the distributions of high and low energy electrons, respectively. The emission from N_2^+ ($B_2\Sigma_u^+ \rightarrow X_2\Sigma_g^+$: λ = 391.4 nm) provided qualitative information about the relative spatial distribution of He* metastable atoms within the discharge gap. The He I line with a threshold energy of 22.7 eV is indicative of high energy electrons or the presence of high electric fields. This line is mainly excited in the cathode layer region and shows a radial spreading of the cathode layer, as shown in Figure 6. Collapse of the cathode layer starting in the discharge center leads to the formation of a ring-like layer that propagates in radial direction late in the discharge pulse. The N_2 emission line at 337.1 nm with a threshold energy of 11.03 eV can be excited by less energetic electrons and is emitted in the positive column region of the discharge, Figure 7. It shows the same feature of a radial expansion of the discharge during the current pulse. The N_2^+ line at 391.4 nm is excited by Penning ionization through metastable helium atoms. It shows that the metastable helium atom density also spreads in radial direction during the discharge pulse but remains maximal on the discharge axis, Figure 8.

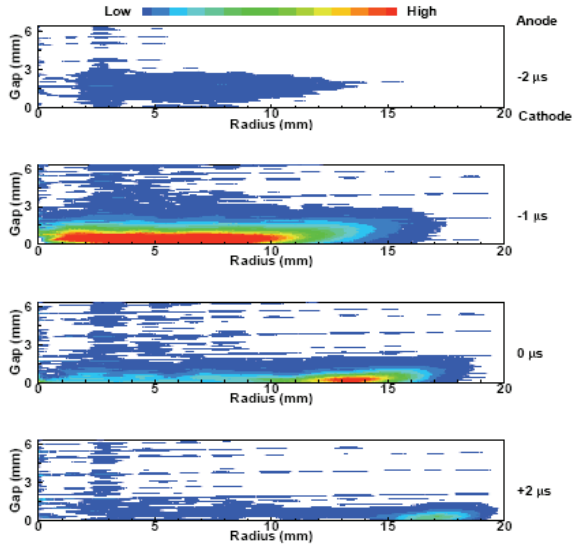

Figure 6: Two-dimensionally resolved spectral emission of the He I ($3s^3S \rightarrow 2p^3P$) 706.5 nm line. Times refer to the maximum of the current pulse.

Another focus of our work was the development of a comprehensive two-dimensional numerical simulation code for the APGD. The model is based on the two-dimensional solution of the species continuity and momentum equations. Species considered are electrons, as well

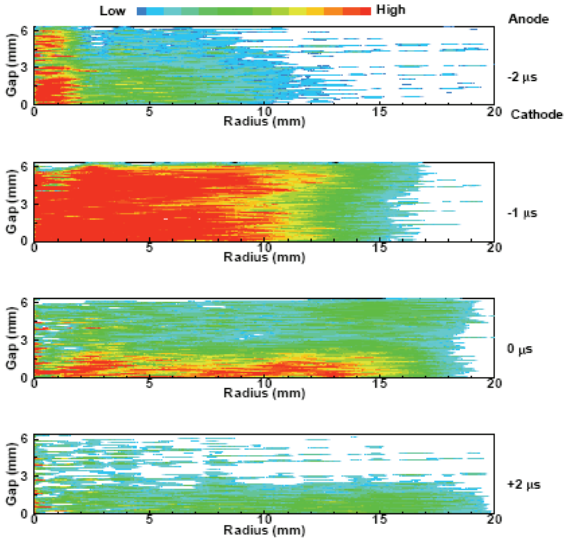

Figure 7: Two-dimensionally resolved spectral emission of the N_2 ($C^3\Pi_u \rightarrow B^3\Pi_g$) 337.1 nm line. Times refer to the maximum of the current pulse.

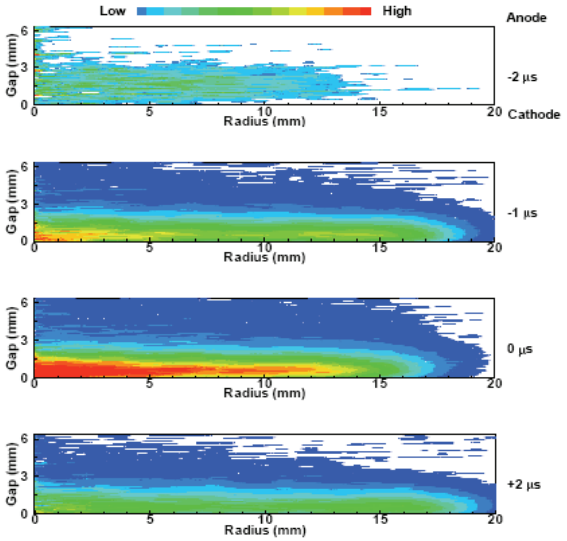

Figure 8: Two-dimensionally resolved spectral emission of the N_2^+ ($B^2\Sigma_u^+ \rightarrow X^2\Sigma_g^+$) 391.4 nm line. Times refer to the maximum of the current pulse.

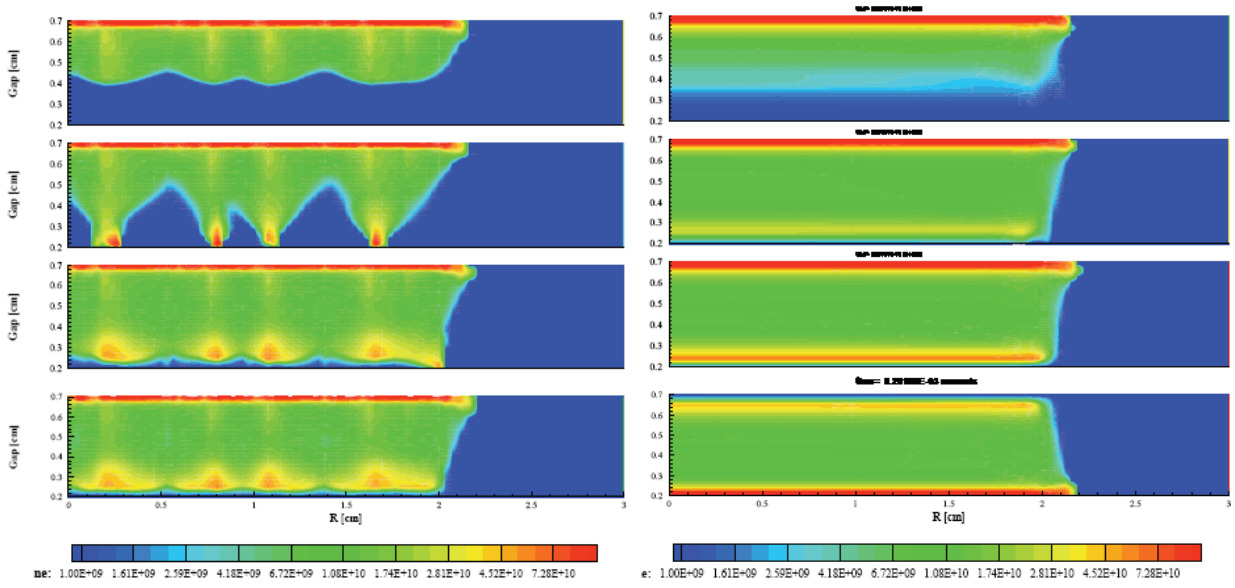

Figure 9: Evolution of the electron density profile for two different driving frequencies of 18 kHz (left) and 30 kHz (right). Other parameters are identical: gap width of 5 mm, two 2-mm alumina dielectrics (dielectric constant = 9), gas is helium at 760 Torr, nitrogen impurity 20 ppm, applied voltage amplitude 1.8 kV.

as neutral and charged helium and nitrogen species. All governing equations are coupled and time-dependent. There are two main challenges for simulating the APGD: First, the problem involves multiple time-scales. For kilohertz driving frequencies, the simulation needs to run for 10-20 voltage cycles (on the order of milliseconds) before reaching a steady state. However, the duration of the plasma initiation period is several tens or hundreds of nanoseconds, during which the electron density, ion density and electric field can change by orders of magnitude. Stability of the simulation requires very small time steps, during certain phases of the discharge as small as 10^{-11}s. Second, in the APGD spatial gradients of the species density are very large as well. During discharge initiation, the electron and ion density can increase by 4 to 5 orders of magnitude along the propagating ionization front. To address these problems, we used a semi-implicit time integration scheme to expedite the time-stepping process. In addition, adaptive time advancement is used based on the temporal gradient of certain physical quantities to increase the efficiency. To cope with steep spatial gradients, the Scharfetter-Gummel exponential scheme is used for discretization of the governing equations.

Figure 9 shows a typical result of this simulation. The particular case studied demonstrates the influence of the driving frequency of the high voltage on the discharge stability. After running the simulation of 20 cycles, the lower frequency case at 18 kHz show filamentation of the discharge, which would correspond to a transition to the filamentary dielectric barrier discharge. At the higher driving frequency of 30 kHz the discharge remains stable and no filamentation is observed. This result is consistent with results found in our experiments and those of others. At lower frequency, the electron density between discharge pulses decreases more strongly prior to the next breakdown. This leads to a smaller overlap of electron avalanches during the next breakdown cycle. The reduced overlap of avalanches finally leads to the formation of filaments as observed in figure 9.

II. Experimental studies of particle transport and charging in plasmas

The focus of the experimental studies was on the observation of nanoparticles in the few nanometer size range for comparison with the modeling studies. Due to the tremendous difficulties in observing nanoparticles of < 10 nm diameter in the plasma, initial experimental studies involved the study of particles that are deposited during the operation of the silane plasma.

To study the particle transport to the electrodes of a capacitively coupled plasma, particles were deposited on samples that were then studied ex-situ by Transition Electron Microscopy (TEM). Because particle formation goes along with the deposition of films, the samples actually contained particles embedded in an amorphous matrix. TEM detection of such small particles is far from trivial and requires careful TEM analysis. Figure 10 shows such embedded nanoparticles as observed with transmission electron microscopy (TEM) and high-resolution TEM (HRTEM). The figure shows a focal series of micrographs, depicting a typical crystalline nanoparticles of approximately 2 nm embedded in an amorphous film. The nanocrystallites show a reversal in contrast as the focus is changed from overfocus, as in Figure 10(A), to underfocus, as in Figure 1(C), while the surrounding amorphous film shows no systematic variation in contrast. This clearly identifies these regions as crystalline particles.

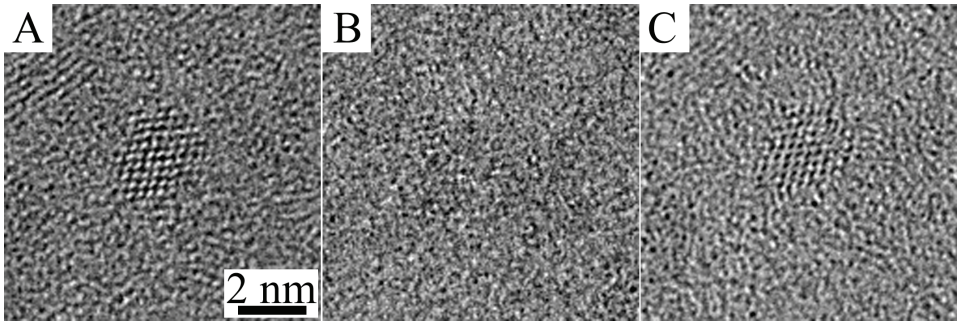

Figure 10. Through-focus HRTEM images of a Si nanoparticle. The contrast of the nanocrystal changes systematically as the focus is changed, while the contrast from the amorphous film is constant in all three images.

Several studies were performed to determine whether the particles observed in the Figure 10 are indeed formed in the plasma or whether they are a result of localized crystallization of the amorphous film. One study to this effect is to use the thermophoretic force acting on particles in the plasma to either allow deposition of the particles or to push them away from the substrate. For

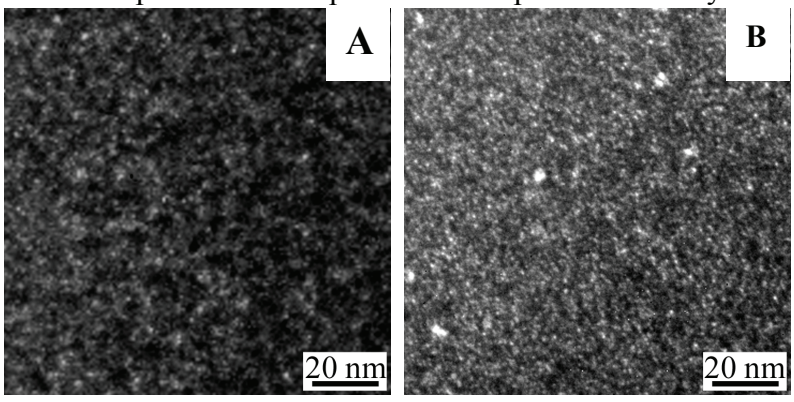

Figure 11. Dark-field TEM images of a film deposited with the 1450 mTorr a/nc-Si:H conditions (A) in the presence of a temperature gradient and (B) standard a/nc-Si:H conditions (both electrodes heated to 250 ^{0}C). The material in (A) appears to be amorphous. No nanocrystals of Si are identifiable in this image. In (B) some nanoparticles approximately 5 nm in size are visible.

this purpose, we deliberately applied a temperature gradient across the RF electrodes. Under the standard a/nc-Si:H conditions both electrodes are heated to 250 C so that no temperature gradient is present. Application of a temperature gradient, for instance, by not heating the electrode opposite to the substrate should push particles away. Figure 11 shows dark-field TEM micrographs of films deposited with a/nc-Si:H plasma conditions (A) with a temperature gradient and (B) with no temperature gradient. The micrograph in Figure 2 (B) shows the typical a/nc-Si:H film structure, with nanocrystallites of approximately 5 nm embedded in an amorphous film matrix. The film shown in Figure 11 (A) appears to be amorphous without any appreciable amount of crystalline material. This provides strong evidence that the particles are indeed formed in the plasma.

Computational modeling of particle nucleation, growth and transport in silane plasmas

We pursued two parallel thrusts in the development of computational models for particle nucleation, growth and transport in silane plasmas: (1) the development of detailed chemical kinetic models that predict particle nucleation, growth and transport in one-dimensional, time-dependent plasmas; and (2) the development of Monte Carlo models to simulate particle transport in three-dimensional, time-dependent plasmas.

1. Detailed chemical kinetic modeling

The goal of this research was to develop a 1D numerical model simulating nanoparticles (formation, growth, and transport) and their influence on the plasma during PECVD. In extending an existing quasi-1D model to quasi-2D, our research has focused on the analysis of our kinetic mechanism, and on the development of 1D plasma and aerosol modules. A reduction analysis was applied to our complex chemistry mechanism to identify species that do not significantly influence the evolution of the system. Results of that analysis identified a set of 98 species that produced essentially the same plasma, chemistry, and nanoparticle characteristics as the initial large set (353 species), for a range of reactor conditions and chemical kinetic parameters. By eliminating unimportant species from the mechanism, computational time is reduced by approximately a factor of ten. Our aerosol model was extended to predict growth and transport of particles in a 1D system. Additionally we developed a 1D RF plasma model, and coupled it with a preliminary aerosol model, accounting for the transport and charging of nanoparticles. In Figure 12, the influence of particles on electron temperature (left) is clear, as the temperature in the sheath increases significantly in the presence of even low particle concentrations (right), compared to the temperature in a pure plasma. The full aerosol model was coupled with the plasma model to predict particle size distributions in addition to the spatial and charge distributions.

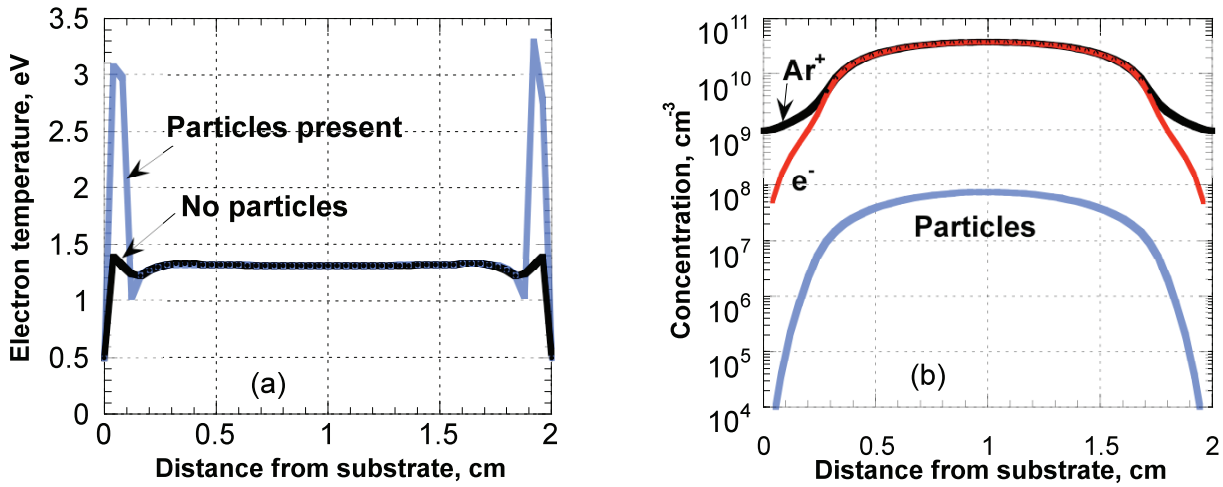

Figure 12. Left: predicted increase in time-averaged electron temperature in plasma sheath, due to low concentrations of particles. Right: predicted concentrations of electrons, ions, and 6-nm-diameter particles.

2. Monte Carlo model of particle transport

We developed a Monte Carlo model to simulate the transport and deposition of nanoparticles in plasmas. Simulations were run for neutral nanoparticles in a 1D reactor and in a 2D axisymmetric low-pressure plasma reactor. Flow in the 2D axisymmetric reactor was modeled using the commercial software CFD-ACE+. A Monte Carlo method was used to simulate collisions between gas molecules and silicon nanoparticles. The time step was taken to be the inverse of the collision frequency of the gas molecules with the nanoparticles. Molecules were assumed to come from a distance of one mean free path away from the particle and the momentum transfer during these collisions is computed. The gas molecules were assumed to have a Maxwellian velocity distribution. The effects of gas drag, gravity and thermophoretic forces on the transport and deposition of nanoparticles was investigated. Gas drag and thermophoresis have predominant effects on the transport of larger nanoparticles whereas the transport of smaller nanoparticles is dominated by diffusion. Parallel computing was taken advantage of in simulating the transport of larger particles at the higher pressures and for larger sample sizes for better understanding of particle transport in the plasma reactor. With parallel computing, the computation time decreases dramatically. Figure 13 shows the transport of nanoparticles in a 2D axisymmetric reactor. Nanoparticles of diameters 10 nm and 50 nm are released in the reactor at time $t = 0$ at random locations. The position of particles at $t = 10$ ms is shown for an argon gas flow rate through the showerhead inlet of 300 sccm. It can be seen that there is a drift of larger particles downward with the gas flow, whereas the smaller nanoparticles are more evenly distributed due to the effect of diffusion.

Jounal Publications sponsored by this grant:

1. "Radial structure of a low frequency atmospheric pressure glow discharge in helium." L Mangolini, K Orlov, U Kortshagen, J Heberlein, and U Kogelschatz, Appl. Phys. Lett. 80, 1722 (2002).

2. "Effects of current limitation through the dielectric in atmospheric pressure glows in helium," L. Mangolini, C. Anderson, J. Heberlein, and U. Kortshagen, J. Phys. D: Appl. Phys. **37**, 1021-1030 (2004).

3. Space and time-resolved emission spectroscopy on atmospheric pressure glows in helium with impurities," C. Anderson, M. Hur, P. Zhang, L. Mangolini, and U. Kortshagen, J. Appl. Phys. **96**(4), 1835-39 (2004).

4. "Observation of Si nanocrystals in a/nc-Si:H films by spherical-aberration corrected transmission electron microscopy," Christopher R. Perrey, Siri Thompson, Markus Lentzen, Uwe Kortshagen, and C. Barry Carter, J. Noncrystalline Solids, **343**, 78-84 (2004).

5. "Observation of Si Nanocrystals by Spherical-Aberration Corrected Transmission Electron Microscopy," Christopher R. Perrey, Julia M. Deneen, Siri S. Thompson, Markus Lentzen, Uwe Kortshagen, and C. Barry Carter, Microscopy and Microanalysis **10** (S02), 996 (2004).

6. "Experimental investigations into the formation of nanoparticles in a/nc-Si:H thin films," S. Thompson, C. R. Perrey, T. J. Belich, J. Kakalios, C. B. Carter, and U. Kortshagen, J. Appl. Physics **97**, 034310 (2005).

7. "Numerical Simulation of Nanoparticle Transport during PECVD," Sarah J. Warthesen, Uwe Kortshagen and Steven L. Girshick, IEEE Transactions on Plasma Science **33**(2), 398-399 (2005).

8. "Atmospheric Pressure Glow Discharge Initiation from a Single Electron Avalanche," Peng Zhang and Uwe Kortshagen, IEEE Transactions on Plasma Science **33**(2), 318-319, (2005).

9. "Two-dimensional Numerical Study of Atmospheric Pressure Glows in Helium with Impurities," P. Zhang, U. Kortshagen, J. Phys. D: Appl. Phys. **39**, 153-163 (2006).

10. "Deposition of vertically oriented carbon nanofibers in atmospheric pressure radio frequency discharge," Tomohiro Nozaki, Tomoya Goto, Ken Okazaki, Kuma Ohnishi, Lorenzo Mangolini, Joachim Heberlein, and Uwe Kortshagen, J. Appl. Phys. **99**, 024310 (2006).

11. "Fabrication of vertically aligned single-walled carbon nanotubes in atmospheric pressure non-thermal plasma CVD," Tomohiro Nozaki, Kuma Ohnishi, Ken Okazaki and Uwe Kortshagen, Carbon **45**, 364-374 (2007).

12. Girshick, S.L. and S.J. Warthesen, *Nanoparticles and Plasmas.* Pure and Applied Chemistry, 2006: p., 78(6), 1109-1116.

13. Warthesen, S.J. and S.L. Girshick, Numerical simulation of the spatiotemporal evolution of a nanoparticle–plasma system. Plasma Chem. Plasma Proc., 2007. 27(3): p. 292-310.